Surface versus internal loading of the Tharsis rise, Mars

Corresponding Author: Anthony R. Lowry

Department of Physics
University of Colorado, Boulder 80309-0390
arlowry@himalaya.colorado.edu
Phone 303 492 5141
Fax 303 492 7935

Shijie Zhong

Department of Physics, University of Colorado, Boulder

Abstract. Two hypotheses compete to explain the remarkable topography and geoid of the Tharsis province on Mars: One attributes Tharsis to volcanically constructed surface loads, whereas the second views it as dynamic effects of single-plume mantle convection. Both are likely to contribute, so we would like to constrain both. We introduce a method to invert load structure from geoid and topography of a viscoelastic planetary body. Estimates of the internal load contribution to Tharsis depend on assumed parameters. Buoyancy of the internal load estimate increases with increasing lithospheric thickness, crustal density and crustal thickness, and load size increases with depth of loading. Despite parameter uncertainties, we can rule out a predominantly internal load. We cannot reject the possibility that Tharsis results from surface loading alone. Internal loads contribute at most 35% of the lithospheric force balance, 50% of the topography and 25% of the geoid at Tharsis, for load depths $\leq$420 km and lithospheric thickness $T_e \leq$200 km. A corollary is that any T_e and reference density structure can exactly reproduce the geoid and topography if internal loading can vary as a function of harmonic degree and order. Hence, T_e and density estimates depend on assumptions about internal loading. If surface and internal loads are approximately uncorrelated, T_e is $\sim$110 km with crustal density $\sim$2600 kg m^{-3}. Adopting these parameters, internal buoyancy contributes 2.1% of lithospheric loading, 4.2% of topography and 0.7% of the geoid at Tharsis for a 200 km deep load, or 4.3% of lithospheric loading, 8.5% of topography and 2.2% of the geoid for a load at 400 km depth.

1. Introduction

The Tharsis rise is easily the dominant feature in the Martian geoid (or areoid), and among topographic features, Tharsis is rivaled only by the extreme topographic contrast between northern lowlands and southern highlands [*Smith et al.*, 1999a, b]. Tharsis occupies about one fifth of the Martian surface area, with an average elevation of more than five km (Figure 1). Several of the highest volcanoes in the solar system are within the Tharsis province, including Olympus Mons at >21 km summit elevation. The entire region is surfaced by shield volcanoes, basaltic lava flows and ignimbrite deposits with ages spanning Noachian to Amazonian time– effectively, the last 4 Gyr of Martian history [*Tanaka et al.*, 1992]. Extensional grabens radiate from the Tharsis rise and from magmatic centers therein, and contractional wrinkle ridges form concentric patterns around the rise [*Tanaka et al.*, 1991]. The density and timing of these features suggests that

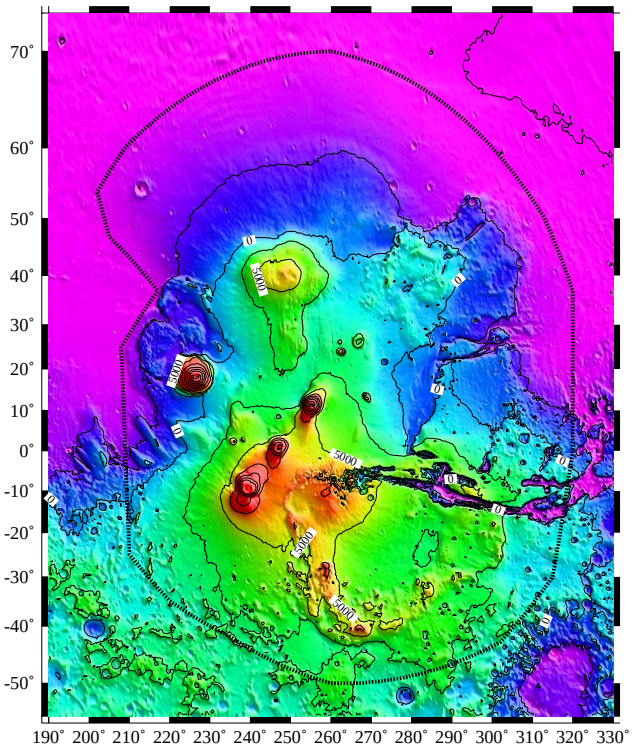

Figure 1. Topographic expression of the Tharsis rise in shaded relief (2500 m contour interval). The thick dotted line delimits the region of mass averaging used to assess lithospheric loading of Tharsis.

the associated lithospheric loading processes peaked in Noachian and generally decreased through time to the Amazonian epoch [*Anderson et al.*, 2001].

The extensive, long-term stationary volcanic activity on Tharsis has prompted two end-member hypotheses for the origins of Tharsis topographic and areoid anomalies. The first hypothesis proposes that the Tharsis rise formed by processes of volcanic construction and shallow magmatic intrusion, and that the areoid and topographic expression reflect the response of an elastic lithosphere to a voluminous volcanogenic load [*Willemann and Turcotte*, 1982; *Solomon and Head*, 1982]. Investigators have cited several observations supporting a predominantly surficial Tharsis in addition to the topography and areoid. For example, most Noachian-aged tectonic structures are well-explained by strain of an elastic lithosphere in reponse to a Tharsis surface load [*Willemann and Turcotte*, 1982; *Banerdt and Golombek*, 2000]. *Phillips et al.* [2001] also relate the distribution of Martian valley networks to fluvial processes responding in part to surface loading of Tharsis.

The surface loading hypothesis assumes that the contribution from internal mass variations is negligible. However, one would expect significant internal mass variations given the thermal and chemical processes implicit for such a large stationary magmagenic system. Consequently, a second hypothesis attributes the Tharsis topography and areoid to thermal buoyancy of a stationary plume in the mantle beneath Tharsis [*Carr*, 1974; *Kiefer et al.*, 1996; *Harder and Christensen*, 1996; *Harder*, 2000] and/or chemical buoyancy of the basalt-depleted residuum [*Sleep and Phillips*, 1979]. Similar to the surface loading hypothesis, distributions of tectonic structures have been cited in support of buoyant internal loading [*Carr*, 1974; *Harder and Christensen*, 1996; *Mege and Masson*, 1996]. Convective models of Martian evolution suggest that a single plume is a natural organizational state given the Martian thermal and phase structure, and continuing volcanism within the Tharsis province [*Hartmann et al.*, 1999] supports the convective modeling conclusion that plume-generated thermal and/or chemical buoyancy is still present today [*Harder and Christensen*, 1996; *Breuer et al.*, 1998; *Harder*, 2000].

Most investigations have examined one hypothesis of Tharsis formation or the other, but it is quite reasonable to expect that both surface and internal loading processes contribute. Synthesis of Tharsis loading studies is complicated by differences in the modeling approaches used to study surface loading and mantle convection: Studies of surface loading generally assume an elastic plate over an inviscid fluid, thus ignoring contributions from the viscous mantle, whereas mantle flow models typically assume a viscous lithosphere or ignore the lithosphere altogether. *Zhong* [2002] introduced a generalized viscoelastic loading model capable of simulating both instantaneous viscous flow and elastic lithospheric responses to surface and internal loads. Using that model, *Zhong* [2002] demonstrated that the areoid expression of plume buoyancy filtered by an elastic lithosphere is significantly smaller than that predicted by purely viscous modeling, implying that surface loading processes must play an important role at Tharsis. *Zhong and Roberts* [2003] extended the analysis to assess possible contributions of a convective thermal plume to the observed areoid and topography at spherical harmonic degrees l=2−3.

Understanding the genesis of Tharsis topography and areoid is key to interpreting the tectonic, volcanic and thermal evolution of Mars [*Solomon and Head*, 1982], and will factor into understanding the evolution of the atmosphere, hydrosphere and surface morphology as

well [*Phillips et al.*, 2001]. The distribution of Tharsis mass remains the largest source of uncertainty in estimates of Martian moment of inertia [*Bills and James*, 1999] and consequently in radii of the core-mantle and crust-mantle boundaries [*Sohl and Spohn*, 1997]. As a first step toward addressing these issues, we introduce a method for inverting the load structure from geoid and topography of a viscoelastic planetary body. We apply the method to spherical harmonic coefficients up to degree and order 60 of the Mars Global Surveyor/Orbital Laser Altimeter (MGS/MOLA) areoid and topography fields [*Smith et al.*, 1999a, b]. The load calculation retains all of the information content (i.e., signs and amplitudes of each individual coefficient) in the estimates of loading, and consequently we are able to examine the loading effects localized to the Tharsis province. We examine relative contributions of surface and internal loading to the Tharsis areoid and topography, and we also explore the range of possible solutions given uncertainties in assumed parameters of Martian density structure and lithospheric thickness.

2. Inverse Modeling of Planetary Loading

In this section, we develop a methodology for separating the effects of surface loading and internal mass anomalies in the areoid and Martian topography. The method significantly extends an inverse approach previously applied to the Cordilleran region of the western United States [*Lowry et al.*, 2000]. We separate the Martian mass structure into three contributions: surface topographic loads h^S, internal mass anomalies ξ which also act as loads, and deflection of the lithosphere w in response to those loads. The three fields h^S, w and ξ are calculated from equations describing flexural isostatic response and the areoid. Notation for the development that follows is provided in Table 1.

2.1. Generalized thin-plate flexure

Following *Turcotte et al.* [1981], we assume a thin spherical elastic shell with outer (planetary) radius R_p and thickness T_e. We generalize the *Turcotte et al.* [1981] formulation slightly to include the effects of internal loading, and we assume the lithosphere surrounds a viscous (rather than inviscid) fluid. The flexural displacement w (positive upward) in response to an applied vertical stress p (positive downward) is governed by [*Turcotte et al.*, 1981; *Willemann and Turcotte*, 1982]:

$$\left[D\nabla^6 + 4D\left(\nabla^4 + \nabla^2\right) + ET_eR_p^2\left(\nabla^2 + 2\right)\right] w = -R_p^4\left(\nabla^2 + 1 - \nu\right) p, \quad (1)$$

in which $D = ET_e^3/[12(1-\nu^2)]$ is flexural rigidity, E is Young's modulus, and ν Poisson's ratio.

The final topography h, flexure w and areoid N re-

Table 1. Notation used in this paper.

Symbol	Description
α	surface deformation response kernel
B_l^2	areoid uncertainty degree variance
$\mathcal{C}$	load amplification test criterion
D	elastic shell flexural rigidity
E	Young's modulus
$\mathcal{F}^I$	resolved force of internal loading
$\mathcal{F}^S$	resolved force of surface loading
g	acceleration of gravity
γ_l	spherical Laplacian operator
γ^2	global coherence of load fields
h	surface topography
h^S	surface load thickness
i	spherical harmonic sin/cos index
$\imath$	imaginary number
l	spherical harmonic degree
$\mathcal{L}$	load amplification limit criterion
m	spherical harmonic order
N	areoid
ν	Poisson's ratio
Ω	polygonal region area
P_{lm}	Legendre polynomials
p	lithospheric load stress
ϕ	longitude
R_1	radius of crust/mantle boundary
R_I	radius of internal loading
R_p	mean planetary radius
ρ_0	crustal density
ρ_1	mantle density
$\mathcal{S}$	load projection scaling factor
$\mathcal{S}^{-1}$	inverse load projection scaling
σ	elastic shell bending resistance
T_e	elastic shell thickness
τ	elastic shell membrane resistance
θ	colatitude
Θ	polar coordinate of load projection
w	flexural deflection
ξ	internal load mass density
Y	spherical harmonics
ζ	polygonal region function

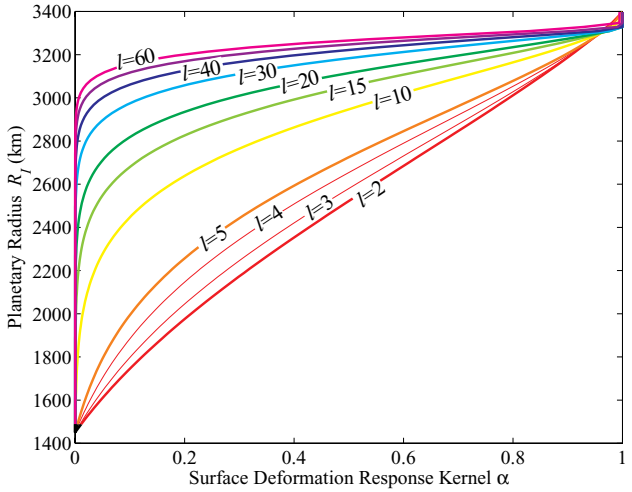

Figure 2. Example surface deformation response kernels $\alpha_l(R_I)$ relative to the areoid for a unit internal load, using model parameters in Table 2.

sult from a combination of surface topographic loading with thickness $h^S = h - w$ and a mass anomaly at the radius of internal loading R_I which has mass per unit area ξ. Coupling between deep internal loads and the elastic lithosphere attenuates with depth below the lithosphere according to the response kernel $\alpha(R_I)$ for surface deformation relative to the areoid. The response kernel, examples of which are shown in Figure 2, is calculated assuming an incompressible flow approximation of a spherically-symmetric, viscous planetary body [*Hager and Richards*, 1989]. Then the thin plate approximation to the vertical load stress is given by

$$p = g\left(\rho_0 h^S + \alpha\xi - \rho_1 N + \rho_1 w\right). \tag{2}$$

Here, the crust has constant density ρ_0 and the mantle ρ_1, and g is gravitational acceleration. *Turcotte et al.* [1981] define the dimensionless parameters

$$\tau \equiv \frac{ET_e}{R_p^2 g\left(\rho_1 - \rho_0\right)}, \tag{3}$$

describing the shell's resistance to deflection due to membrane stress, and

$$\sigma \equiv \frac{D}{R_p^4 g\left(\rho_1 - \rho_0\right)}, \tag{4}$$

describing the bending stress resistance. For convenience of notation, we define τ' and σ' to be the parameters (3) and (4), respectively, multiplied by $\rho_1 - \rho_0$. Then equations (1) and (2) become

$$\left[\sigma'\left(\nabla^6 + 4\nabla^4 + 4\nabla^2\right) + \tau'\left(\nabla^2 + 2\right)\right] w$$
$$= -\left(\nabla^2 + 1 - \nu\right)\left[\rho_0 h^S + \alpha\xi - \rho_1\left(N - w\right)\right]. \tag{5}$$

We express the spatially varying fields in equation (5) in the spherical harmonic domain where, for example,

$$\left\{\begin{array}{c} h(\theta,\phi) \\ w(\theta,\phi) \\ N(\theta,\phi) \end{array}\right\} = \left\{\begin{array}{c} \sum_{i,l,m} h_{ilm} Y_{ilm}(\theta,\phi) \\ \sum_{i,l,m} w_{ilm} Y_{ilm}(\theta,\phi) \\ \sum_{i,l,m} N_{ilm} Y_{ilm}(\theta,\phi) \end{array}\right\} \tag{6}$$

in which θ is colatitude, ϕ is longitude,

$$Y_{ilm}(\theta,\phi) = P_{lm}(\cos\theta)\left\{\begin{array}{c} \cos m\phi; i = 1 \\ \sin m\phi; i = 2 \end{array}\right\}, \tag{7}$$

P_{lm} are the Legendre and associated Legendre polynomials normalized to 4π (geodesy normalization), and h_{ilm}, w_{ilm} and N_{ilm} are the spherical harmonic coefficients of the topography, flexural deflection and areoid respectively. In the spherical harmonic domain, the Laplacian operator ∇^2 acts on Y_{ilm} as

$$\nabla^2 Y_{ilm}(\theta,\phi) = -\gamma_l Y_{ilm}(\theta,\phi). \tag{8}$$

in which $\gamma_l \equiv l(l+1)$. Substituting, the flexural relation becomes

$$-\{\sigma'\left[\gamma_l^3 - 4\gamma_l^2 + 4\gamma_l\right] + \tau'\left[\gamma_l - 2\right] + \rho_1\left[\gamma_l - (1-\nu)\right]\} w_{ilm}$$
$$= \left[\gamma_l - (1-\nu)\right]\left(\rho_0 h^S_{ilm} + \alpha_l \xi_{ilm} - \rho_1 N_{ilm}\right). \tag{9}$$

2.2. Finite-amplitude areoid response

The areoid height N due to a finite amplitude topography H on some interface with density change $\Delta\rho$ can be expressed as [*Wieczorek and Phillips*, 1998]

$$N(\theta,\phi) = 2\pi G \sum_{i,l,m}\left(\frac{r}{R_p}\right)^{l+1} \frac{2r\Delta\rho}{g\left(2l+1\right)}$$
$$\cdot\left[H_{ilm} + \sum_{n=2}^{l+3} \frac{H^n_{ilm}\prod_{j=2}^{n}\left(l+4-j\right)}{r^{n-1}n!}\right] Y_{ilm}(\theta,\phi) \tag{10}$$

in which G is the gravitational constant, r is the reference radius of the topography, and H^n_{ilm} are the spherical harmonic coefficients of the topography raised to the n^{th} power, $H^n(\theta,\phi)$. Here we have adopted the separation of the areoid equation into linear and nonlinear (i.e., higher order in the Taylor series) terms, as suggested by *McKenzie et al.* [2002]. Equation (10) differs from that in *McKenzie et al.* [2002] by a factor of r^{1-n} in the higher-order terms, correcting an apparent typographical error therein.

Table 2. Parameters of the reference model of Martian loading.

Parameter	Symbol	Value	Source
Planetary radius	R_p	3397 km	(1)
Crustal density	ρ_0	2900 kg/m^3	(2)
Mantle radius	R_1	3347 km	(2)
Mantle density	ρ_1	3400 kg/m^3	(2)
Gravitational acceleration	g	3.71 m/s	(1)
Elastic shell thickness	T_e	100 km	
Young's modulus	E	1.44×10^{11} Pa	(3)
Poisson's ratio	ν	0.268	(3)

(1) *Lemoine et al.* [2002]
(2) *Zuber et al.* [2000]
(3) *McKenzie et al.* [2002]

2.3. Load deconvolution

Equations (9) and (10), coupled with the definition of the surface load $h^S \equiv h - w$, comprise a system of three equations in the three unknowns h^S, ξ and w. The areoid calculation depends nonlinearly on both the observed surface topography h and the unknown flexure w, so we write these equations with the higher order terms in w placed on the right-hand-side as

$$\begin{bmatrix} 1 & 1 & 0 \\ 0 & C_2 & C_3 \\ \rho_0 K_1 & K_2 & \alpha_l K_1 \end{bmatrix} \begin{bmatrix} h^S_{ilm} \\ w_{ilm} \\ \xi_{ilm} \end{bmatrix} = \begin{bmatrix} h_{ilm} \\ N_{ilm} - C_1 h_{ilm} - \sum_{n=2}^{l+3} \left(C_1^n h_{ilm}^n + C_2^n w_{ilm}^n\right) \\ \rho_1 K_1 N_{ilm} \end{bmatrix}. \quad (11)$$

Here we have defined

$$C_1 = \frac{4\pi G R_p \rho_0}{g(2l+1)}; \quad (12)$$

$$C_1^n = C_1 \frac{\prod_{j=2}^{n}(l+4-j)}{R_p^{n-1} n!}; \quad (13)$$

$$C_2 = \frac{4\pi G R_1 (\rho_1 - \rho_0)}{g(2l+1)} \left(\frac{R_1}{R_p}\right)^{l+1}; \quad (14)$$

$$C_2^n = C_2 \frac{\prod_{j=2}^{n}(l+4-j)}{R_1^{n-1} n!}; \quad (15)$$

$$C_3 = \frac{4\pi G R_I}{g(2l+1)} \left(\frac{R_I}{R_p}\right)^{l+1}; \quad (16)$$

$$K_1 = \gamma_l - (1-\nu); \quad (17)$$

$$K_2 = \{\sigma'[\gamma_l^3 - 4\gamma_l^2 + 4\gamma_l] + \tau'[\gamma_l - 2] + \rho_1 K_1\}, \quad (18)$$

and R_1 is the mean radius of the crust/mantle boundary. Equations (11) are solved iteratively for each coefficient (i, l, m). During the first iteration the higher-order terms in w on the right-hand-side are set to zero, and these terms are updated at each subsequent iteration until a convergence criterion is achieved. In calculations presented here, we consider the solution converged when the average percentage change in areoid coefficients is less than 0.1%. Given the observed topography and areoid, and assuming a "known" density structure, lithospheric thickness and internal loading depth, we can uniquely solve equations (11) for the unknown surface load thickness h^S, internal load mass ξ, and lithospheric flexure w.

2.4. Singularity

Solution of the system of equations (11) converges within one to three iterations so long as the linear system is not close to singular for any $l \leq 60$. Setting the determinant of the sensitivity matrix in (11) equal to zero and solving, one finds that a singular load deconvolution matrix results if the internal load radius

$$R_I^{\mathrm{Sing}} = R_1 \left[\frac{\alpha_l (\rho_1 - \rho_0) K_1}{K_2 - \rho_0 K_1}\right]^{\left(\frac{1}{l+2}\right)}. \quad (19)$$

One can readily show that when the matrix is singular, the ratio of areoid to topography coefficients,

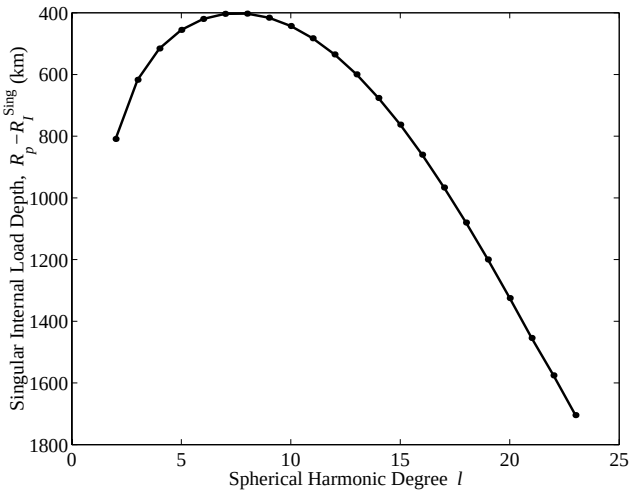

Figure 3. Internal load depths resulting in singularity of load deconvolution, for model parameters in Table 2.

N_{ilm}/h_{ilm}, for pure surface loading is identical to that for pure internal loading. Hence, the relative contributions of internal and surface loading are indeterminate if both yield the same relationship of areoid to topography. Figure 3 depicts singular depths of internal loading for a reference model of Mars described in Table 2. The N/h ratios predicted for both internal loading and surface loading depend on T_e, density structure and spherical harmonic degree. N/h for internal loading is also very sensitive to the assumed loading depth and varies significantly between the surface and the core-mantle boundary. Consequently, a radius of singularity will occur somewhere within the mantle for l less than about 25. For the reference model parameters, the shallowest singular load depth occurs for l=7 to 8 at about 400 km, which is within the range of depths that may be relevant for internal loading by a degree-1 plume structure under Tharsis.

Near-singularity of the load deconvolution matrix (11) can produce highly spurious estimates of load mass if the assumed depth of internal loading is significantly different than the true load depth. Singularity of the load deconvolution matrix on the left-hand-side of equations (11) is a mathematical artifact stemming from the assumption that internal loading occurs at a single, fixed radius. In reality, planetary internal loading is distributed over a range of depths, reflecting the influence of various dynamical processes on the chemistry, temperature and phase of materials. However, we cannot adequately constrain a vertically distributed

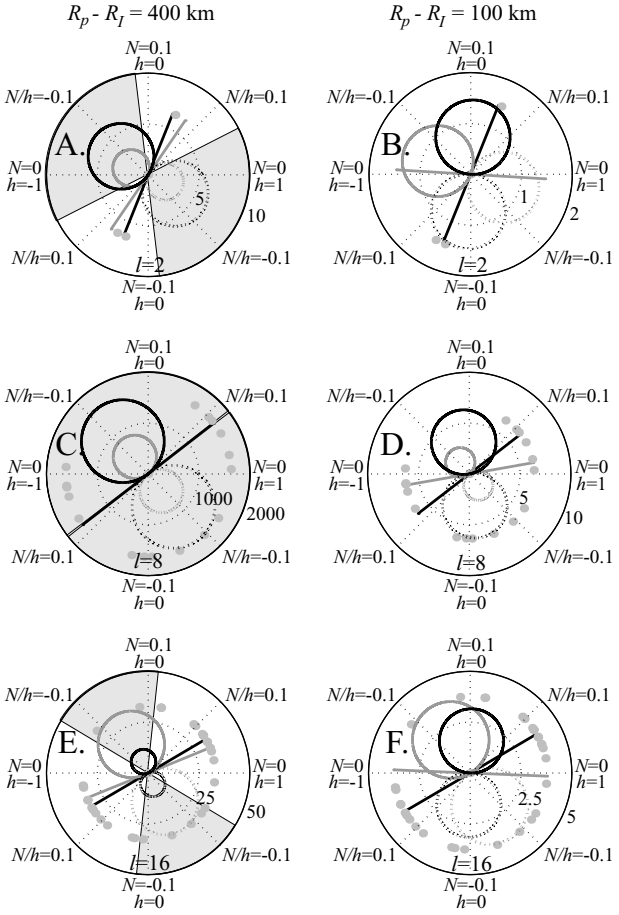

Figure 4. Inverted loads for model parameters in Table 2. Topography and areoid map to the Θ-axis of polar projection as $\tilde{h} = \cos\Theta; \tilde{N} = 0.1\sin\Theta$. The resulting loads are plotted on the radial axis. Black curve is surface load, h^S, and gray is the height equivalent of the internal load, ξ/ρ_0, in meters. Positive loading is solid and negative is dotted. The black bar denotes pure surface loading ($\xi = 0$); the gray bar pure internal loading ($h^S = 0$). Light gray filled circles correspond to observed N/h coefficient ratios of Mars data. Very light gray shading indicates Θ for which the load amplitude criterion $\mathcal{C} > 1$. Note the radial axis scale varies significantly in each plot. (a) l=2; internal load depth $R_p - R_I$=400 km, (b) l=2; $R_p - R_I$=100 km, (c) l=8; $R_p - R_I$=400 km, (d) l=8; $R_p - R_I$=100 km, (e) l=16; $R_p - R_I$=400 km, (f) l=16; $R_p - R_I$=100 km.

loading structure from the areoid and topography data alone, and in the absence of other data it is reasonable to approximate internal loading as occurring at a single depth. Unfortunately, when the load deconvolution

matrix in (11) is nearly singular, the iterative solution of equations (11) may not converge. Consequently, we must assess whether a particular estimate of load amplitude approximately represents the true load distribution as opposed to a mathematical singularity.

In Figure 4, we plot curves demonstrating the dependence of the surface load, h^S, and the internal load scaled by crustal density, ξ/ρ_0, on the areoid/topography ratio for various l and loading depths. Load coefficients were calculated for N/h coefficient relationships encompassing $h = \cos\Theta; N = 0.1\sin\Theta$ for Θ in the range $[0, 2\pi]$. Here, Θ is a dummy coordinate of the polar projection, and we have used equations (11) to calculate the surface loads and internal loads for a large number of different values of Θ in order to produce the curves shown in Figure 4. We use $N = 0.1\sin\Theta$ instead of the unit circle to better visually distinguish effects of loading (and because areoid coefficients are typically one to two orders of magnitude smaller than Martian topography coefficients). The example calculations use the reference model in Table 2 and internal load depths of 400 and 100 km. In most cases shown in Figure 4, the maximum load amplitudes are relatively small (from 1 to 30 meters). However, for l=8 and $R_p - R_I$=400 km, the maximum possible load size is much larger, by several orders of magnitude. l=8 and $R_p - R_I$=400 km yields a nearly singular load deconvolution matrix (compare with Figure 3; the actual $R_p - R_I^{\mathrm{Sing}}$ is 402.5 km).

The maximum amplitudes of loads inverted on the $h = \cos\Theta; N = 0.1\sin\Theta$ circle of projection is depicted for all l = 2 to 60 for a 400 km internal load depth in Figure 5a, and for a 100 km load depth in Figure 5b. Two effects can amplify the calculated load coefficients to physically unlikely values. One is downward continuation of the areoid to calculate mass sources at the depth of internal loading. Downward continuation amplifies the mass anomaly at depth R_I by a factor of $(R_p/R_I)^{l+1}$ relative to the mass anomaly at the planetary surface that would yield the same geoid anomaly. The effects of this amplification on the calculated internal load at large l can be seen by comparing the estimate of equivalent internal load height (solid gray line) with the load divided by the continuation factor (dashed) in Figure 5. The second effect, noted previously, is near-singularity of the load deconvolution matrix, which can amplify both loads by several orders of magnitude when the assumed internal load radius is near the singular load radius R_I^{Sing}.

As noted earlier, the coefficient ratio N/h predicted for pure surface loading is identical to that for pure internal loading when the load deconvolution matrix

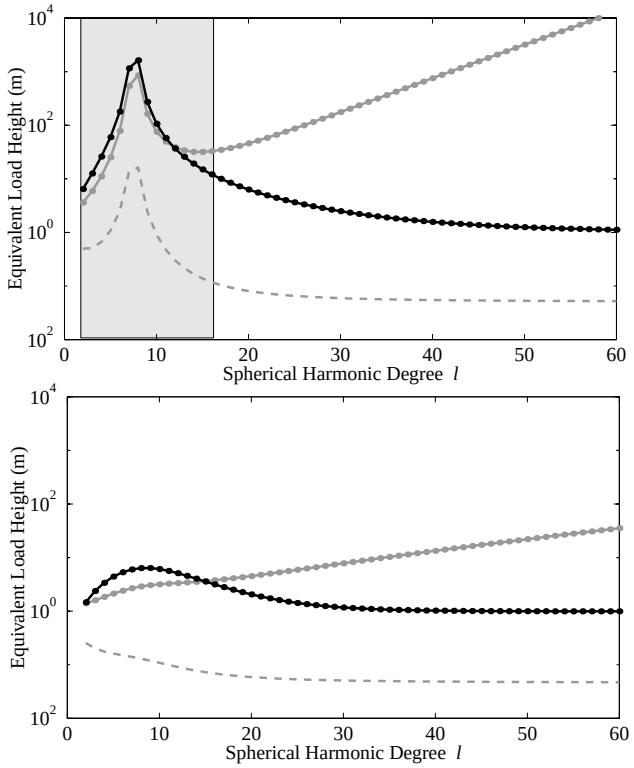

Figure 5. Maximum inverted load coefficients for model parameters in Table 2 and projected topography $\tilde{h} = \cos\Theta$ and areoid $\tilde{N} = 0.1\sin\Theta$. Black line with filled circles is the maximum surface load h^S; solid gray line is the internal load height ξ/ρ_0. Dashed gray lines are the maximum internal load scaled by the areoid continuation factor, $\xi(R_I/R_p)^{l+1}/[\rho_0(2l+1)]$. Very light gray shading indicates l for which the load amplitude criterion $\mathcal{C}$ can exceed one. (a) Internal load depth $R_p - R_I$=400 km, (b) $R_p - R_I$=100 km.

is singular. If the assumed load radius exactly equals R_I^{Sing}, no solution is possible, but this is an unlikely occurrence. However, in the examination of Tharsis loading that is the subject of this paper, reasonable assumptions of internal loading radius commonly fall near the singular radius for some range of l. Extreme amplification of estimated loads occurs when the matrix (11) is nearly singular and the observed N/h is very different than that predicted for pure surface loading (e.g., Figure 4c). If significant loading really does occur near R_I^{Sing} for a particular spherical harmonic coefficient, N_{ilm}/h_{ilm} should approximately equal the coefficient ratio predicted for pure surface loading, in which case the load amplitudes predicted by deconvolution will be physically reasonable. If coefficient ratios are not near

the value of N/h predicted for pure surface loading, however, it is likely that internal loading has significant contributions from some other radii besides R_I^{Sing}. Hence, we enforce limits on load amplitudes at those particular combinations of R_I, l and N/h which would otherwise yield unreasonably large load coefficients.

The algorithm to identify physically unreasonable amplification of loads at near-singular load radii proceeds via the following steps:

1. We determine where the observed areoid and topography coefficients would project onto the $(\tilde{h} = \cos\Theta; \tilde{N} = 0.1\sin\Theta)$ circle via

$$\Theta_{ilm} = \tan^{-1}\left(\frac{10N_{ilm}}{h_{ilm}}\right). \tag{20}$$

The observed coefficients project onto the circle via multiplication by a scaling factor $\mathcal{S}_{ilm}$: $[\tilde{h}_{ilm}, \tilde{N}_{ilm}] = \mathcal{S}_{ilm}\,[h_{ilm}, N_{ilm}]$, where $\mathcal{S}_{ilm} = \cos\Theta_{ilm}/h_{ilm}$.

2. We multiply the right-hand-side of equations (11) by $\mathcal{S}_{ilm}$, and then we solve the system of equations for $[\tilde{h}^S_{ilm}, \tilde{w}_{ilm}, \tilde{\xi}_{ilm}]$. Here the tilde denotes the solution on the $(\tilde{h} = \cos\Theta; \tilde{N} = 0.1\sin\Theta)$ circle of polar projection, as distinct from the solution using the observed areoid and topography coefficients.

3. We define a test criterion $\mathcal{C}$ to identify physically unrealistic amplification of the load amplitudes, given by

$$\mathcal{C}_{ilm} \equiv \frac{\tilde{h}^S_{ilm}\tilde{\xi}_{ilm}}{\rho_0(2l+1)}\left(\frac{R_I}{R_p}\right)^{l+1} \tag{21}$$

Note that this is simply the product of the projected surface load and internal load height scaled by the upward continuation of the areoid in equation (16): I.e., the dashed gray line in Figure 5 multiplied by the black line.

4. We assign a scaling factor to map back from the circle of polar projection to the original N_{ilm}, h_{ilm} coefficients based on whether the test criterion $\mathcal{C}_{ilm}$ exceeds an empirically defined limit $\mathcal{L}$:

$$\mathcal{S}^{-1}_{ilm} = \left\{ \begin{array}{ll} \frac{1}{\mathcal{S}_{ilm}}, & \mathcal{C}_{ilm} \le \mathcal{L} \\ \frac{\mathcal{L}}{\mathcal{C}_{ilm}\mathcal{S}_{ilm}}, & \mathcal{C}_{ilm} > \mathcal{L} \end{array} \right\} \tag{22}$$

5. We multiply the solution vector $[\tilde{h^S}_{ilm}, \tilde{w}_{ilm}, \tilde{\xi}_{ilm}]$ by $\mathcal{S}^{-1}_{ilm}$ to arrive at the final solution.

The projection method described above has three important features: (1) By projecting the observed coefficients onto the $(\tilde{h} = \cos\Theta; \tilde{N} = 0.1\sin\Theta)$ circle, near-singular load amplification is identified independently of the absolute amplitudes of the areoid and topography. (2) If the assumed loading depth is near the singular depth, but the observed areoid-topography coefficient ratio closely approximates the ratio expected for loading at that depth, the test criterion will not exceed the empirically defined limit. (3) If the test criterion does exceed the limit for a particular coefficient pair, the algorithm preserves the ratio of predicted internal to surface loading $\xi_{ilm}/\rho_0 h^S_{ilm}$ while the load coefficients themselves are reduced. The resulting load coefficients are reduced enough to guarantee convergence of the solution of equations (11), but can still be so large as to be physically implausible.

We tested the projection approach for a range of choices of the limit criterion $\mathcal{L}$. $\mathcal{L}$=1 was found empirically to be the largest choice of $\mathcal{L}$ which guaranteed convergence of the iterative solution of equations (11) for all model parameterizations considered in this paper. Consequently, most of the calculations presented in the remainder of this paper use $\mathcal{L} = 1$. Example conditions for which the test criterion $\mathcal{C}$ can exceed $\mathcal{L}$=1 are indicated by light gray shading in Figures 4 and 5. The test criterion for the 400 km load depth in Figure 5a can exceed the limit for certain areoid-topography ratios when l=2−17. For the 100 km load depth example shown in Figure 5b, the test criterion never exceeds the limit. In the case of a 400 km load depth, the range of Θ for which $\mathcal{C} > 1$ does not include any of the observed Martian coefficient ratios when $l = 2$ (Figure 4a), but almost all of the load coefficients would be reduced for $l = 8$ (Figure 4c) and about 10% would be reduced for $l = 16$ (Figure 4e). We will compare solutions using $\mathcal{L}$=1 with convergent solutions using $\mathcal{L}$=∞ (i.e., with unlimited load amplitudes) in section 5.

2.5. Load integration for the Tharsis region

Much of the controversy surrounding loading processes of the Tharsis rise centers on how much of the topographic expression results from internal loading by plume buoyancy, and how much from surface loading by volcanic construction. Hence, once the load mass fields have been estimated for the planet, we would like to examine loading localized to the Tharsis region in particular, as well as the sensitivity of load estimates to *a priori* assumptions of lithospheric thickness, depth of internal loading, and density structure of Mars. Toward this end, we integrate the stresses applied by internal and surface loads to estimate a resolved force for Tharsis loading.

We modify a method for estimating regionally averaged surface mass from time-variable geoid anomalies [*Swenson and Wahr*, 2002] to estimate resolved forces within the Tharsis region. Error in an estimate of re-

gionally averaged surface mass density, $\bar{\sigma}_{region}$, is minimized by

$$\bar{\sigma}_{region} = \sum_{i,l,m} \frac{\Upsilon_l}{\Omega_{region}} W_{ilm} N_{ilm}. \quad (23)$$

Here, Ω_{region} is the area of the region of interest, Υ_l is the transfer function that relates surface mass density coefficients to areoid coefficients, and W_{ilm} are optimized weight coefficients [*Swenson and Wahr*, 2002]

$$W_{ilm} = \left[1 + \frac{2\Upsilon_l^2 B_l^2}{\sigma_0^2 G_l (2l+1)}\right]^{-1} \zeta_{ilm} \quad (24)$$

in which B_l^2 is the degree variance of the satellite areoid measurements, σ_0^2 is the variance of the expected mass signal, G_l are coefficients of the spatial covariance of the expected signal, and ζ_{ilm} are coefficients of a region function $\zeta(\theta, \phi)$ which has value one inside the region of interest and zero outside. We modify (23) to estimate a resolved force, i.e., the integral of stress over the region as opposed to the average of mass density. Substituting the appropriate relations, we get

$$\mathcal{F}^S = \rho_0 g \sum_{i,l,m} \left[1 + \frac{2B_l \rho_0^2}{\sigma_0^2 G_l C_1^2 (2l+1)}\right]^{-1} \zeta_{ilm} h^S_{ilm} \quad (25)$$

for the resolved force of surface loading, and

$$\mathcal{F}^I = g \sum_{i,l,m} \alpha_l \left[1 + \frac{2B_l}{\sigma_0^2 G_l C_3^2 (2l+1)}\right]^{-1} \zeta_{ilm} \xi_{ilm} \quad (26)$$

for the resolved force of internal loading.

To evaluate the relative importance of internal versus surface loading processes in the topographic signature of Tharsis, we will express these resolved forces as a percentage ratio describing the internal loading relative to total loading via $-100\mathcal{F}^I/(|\mathcal{F}^S| + |\mathcal{F}^I|)$. The ratio includes a negative sign for the resolved force of internal loading because we expect predominantly buoyant (i.e., negative) internal loading by hot plume material and/or iron-depleted melt residuum. If the sign of the internal load is positive (i.e., anomalously dense), the resulting percentage will be negative.

For calculations presented here, we use the region depicted in Figure 1 to generate the coefficients ζ_{ilm}. The degree variance of satellite measurement uncertainty B_l^2 was calculated from individual areoid coefficient uncertainties δ_{ilm} [*Frank Lemoine, personal communication*, 2002] via

$$B_l^2 = \sum_{i,m} \frac{\delta_{ilm}^2}{2l+1}. \quad (27)$$

The statistical properties of mass density, σ_0^2 and G_l, were approximated from the observed Martian topographic field $h(\theta, \phi)$.

2.6. Internal contributions to areoid and topography

In addition to knowing the relative sizes of surface and internal loading, it is desirable to define an estimate of the percentage internal and surface load contributions to the observed topography and areoid. The spatial average of topography $\bar{\mathcal{H}}$, for example, is

$$\bar{\mathcal{H}}_{\text{Tharsis}} = \sum_{i,l,m} \frac{\zeta_{ilm}}{\Omega_{\text{Tharsis}}} h_{ilm}. \quad (28)$$

We represent the percentage internal load contributions to topography and areoid as $100\bar{\mathcal{H}}^{\mathcal{I}}/\bar{\mathcal{H}}$ and $100\bar{\mathcal{N}}^{\mathcal{I}}/\bar{\mathcal{N}}$. Here, because the flexure w in equations (11) is a lithospheric response to combined internal and surface loading, we calculate the averages for the internal contributions $\bar{\mathcal{H}}^{\mathcal{I}}$ and $\bar{\mathcal{N}}^{\mathcal{I}}$ from the internal load coefficients using

$$h^I_{ilm} = \frac{(\rho_1 C_3 - \alpha_l) K_1}{K_2 - \rho_1 K_1 (C_1 + C_2)} \xi_{ilm} \quad (29)$$

and

$$N^I_{ilm} = \left[C_3 + \frac{(\rho_1 C_3 - \alpha_l) K_1}{K_2 (C_1 + C_2) - \rho_1 K_1}\right] \xi_{ilm}. \quad (30)$$

3. Data Sources

In the following analysis, we use the MGM1004D areoid and associated errors to spherical harmonic degree 60 [*Lemoine et al.*, 2001] and the IEGDR-L3-V1.0 planetary radius data (0.25 degree resolution) archived at http://wwwpds.wustl.edu. The areoid solution is derived from Mars Global Surveyor (MGS) X band tracking data and Mars Orbital Laser Altimer (MOLA) crossovers. Uncertainty in the areoid ranges from 1.0 m at the south pole to 2.6 m near the equator, for harmonics up to l, m=60. In *Smith et al.* [1999a], a distinction is made between planetary "shape" (corresponding to the radius of the planetary surface from the center of mass) and "topography" (corresponding to the height of the planetary surface above the areoid). For the analysis described in section 2, the term "topography" follows another definition used, e.g., in *Turcotte et al.* [1981] and *Wieczorek and Phillips* [1998], in which h is referenced to radius R_p. The latter definition of topography (i.e., the "shape" of *Smith et al.* [1999a]) is the usage of the term followed throughout this paper, and

hence the planetary radius data are used in the following analysis. We subtracted the reference ellipsoid of the MGM1004D areoid (R_p=3397 km and inverse flattening $1/f$ = 191.1372 m) from the mean planetary radius field in the IEGDR data set, and we use the spherical harmonic representation of the resulting topographic field up to degree and order l, m=60 for calculations in this paper. To avoid errors associated with reference frame differences of the topographic and areoid fields, we ignore the (l=2,m=1) and $l \leq 1$ terms in the isostatic analyses presented here. Hydrostatic effects of Martian rotation in the (l=2,m=0) coefficients are largely removed by subtraction of the reference ellipsoid, and so we include those coefficients in the analysis.

4. Results

4.1. Synthetic tests of the method

We tested independently the accuracy of the forward relations (9) for thin shell flexure, (10) for the areoid, and the inversion for loads (11) against a propagator-matrix formulation of viscoelastic response to planetary loading [*Zhong*, 1997; *Zhong and Zuber*, 2000; *Zhong*, 2002]. We compared results for three loading scenarios, including a unit load at the surface (h^S=1 meter), a unit load at 80 km depth ($\xi = \rho_1$ kg m^{-2}), and a unit load at 400 km depth. The synthetic model parameters were identical to those given in Table 2, excepting that both the viscoelastic propagator matrix model and the thin shell model described in this paper used a lithospheric Poisson's ratio of 0.5 to match the instantaneous viscous flow modeling assumption of an incompressible fluid [*Hager and Richards*, 1989].

The forward model of the areoid used the flexure and topography output by the viscoelastic propagator matrix model and a linearized relation (i.e., higher order terms in equation (10) were ignored). The differences between the two are largest for small l and deep internal loads, but nevertheless always less than 1% of the areoid. The differences reflect only the deformation of the core/mantle boundary (CMB), which is included in the viscoelastic model of *Zhong and Zuber* [2000] but ignored in the thin elastic shell model. The forward model of surface topography using equation (9) used the areoid output by the viscoelastic propagator matrix model, so that we could examine errors introduced by equation (9) independent of the CMB contribution to the areoid. Differences between (9) and the viscoelastic propagator matrix model do not exceed 0.5%. These differences represent the effects of the thin shell approximation in (9) plus the instantaneous viscous flow approximation

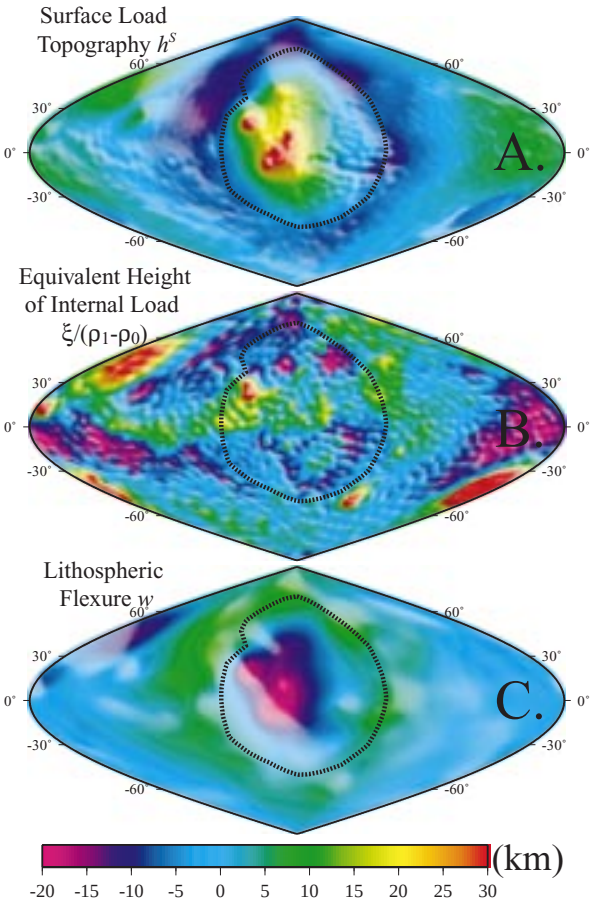

Figure 6. Example solution for (a) surface load h^S, (b) internal load height ξ/ρ_0, and (c) lithospheric flexure w, assuming the reference model in Table 2 and an internal load depth of 50 km.

of viscoelastic coupling α_l between deep loads and the surface. Finally, the unit loads input to the viscoelastic propagator matrix model of *Zhong and Zuber* [2000] were compared with the loads recovered from solution of equations (11) using the areoid and topography output by the viscoelastic model. The combination of errors that arise from ignoring CMB deformation, thick plate effects, and the instantaneous viscous flow approximation of α introduces inaccuracies of at most 5% in the inverted load estimates.

4.2. Reference loading model

An example solution for Martian planetary loading is shown in Figure 6. The calculation assumes the reference density structure and T_e=100 km in Table 2, plus a 50 km depth of internal loading (i.e., at the crust-mantle

boundary). The estimate of surface load h^S (Figure 6a) is dominated by a significant thickness, average 17.8 km, of topographically constructed material within the Tharsis region. The internal load height ξ/ρ_0 (Figure 6b) is dominated by high-frequency variations, some of which probably reflect a factor of $(R_p/R_I)^{l+1}$ amplification by downward continuation of near-surface density variations to the assumed depth of loading. The average of the internal load over Tharsis is positively buoyant but small, equivalent to a height of just 0.5 km. Consequently, the net flexural response of the lithosphere under Tharsis is downward (averaging 12.7 km over the region; Figure 6c). Using the calculations described in sections 2.5 and 2.6, the internal contribution to lithospheric loading of Tharsis is 2.5%, and the internal contributions to topography and the areoid are 6.8% and −0.5%, respectively.

4.3. Model parameter sensitivity

The model used to invert for Tharsis loading depends on properties of the Martian lithosphere and density structure which are only approximately known. A complete analysis of Tharsis loading should include uncertainties, which in this application are dominated by uncertainties in these model parameters. We have defined scalar expressions for the averaged contribution of internal mass anomalies to total lithospheric loading in section 2.5, and to observed areoid and topography in section 2.6. In this section, we explore the dependence of these integral expressions of Tharsis loading on model parameters, including the range of Tharsis loading that is feasible given parameter uncertainties.

Parameters which significantly affect the estimates of internal load contribution include the radius of internal loading R_I and the lithospheric thickness T_e. Internal loading of Tharsis likely reflects three processes: (1) thermal variations generated by the single-plume Martian convective structure [*Harder and Christensen*, 1996], (2) mantle chemical variations introduced by melt depletion [*Sleep and Phillips*, 1979], and (3) crustal chemical variations resulting from magmatic intrusion [*Kiefer*, 2003]. The method presented here cannot distinguish between different types of internal loading, and so all of these are integrated into the final estimate of internal load mass anomaly. Consequently, we consider models for internal loading depths ranging from near the planetary surface to >400 km. Most convective buoyancy of a single-plume structure in the Martian mantle would express just below the lithosphere, at depths shallower than 400 km [*Zhong*, 2002]. Small buoyancy contributions from greater depth are expected, but equations (11) neglect deformation of the core-mantle boundary and so are inaccurate for loading depths much greater than 400 km.

Lithospheric thickness estimates for Mars are highly variable. *McKenzie et al.* [2002] report T_e estimates in the range 12−70 km, while *Zuber et al.* [2000] and *McGovern et al.* [2002] tally estimates ranging from 5 to 200 km. *Nimmo* [2002] estimated T_e across the Martian crustal dichotomy to be ∼60 km, and *Turcotte et al.* [2002] estimated the global Martian T_e=90 km. Generally, low estimates of T_e are derived from impact structures and the most ancient features, whereas the highest values tend to derive from young volcanic features, presumably reflecting planetary cooling with time [*Zuber et al.*, 2000; *McGovern et al.*, 2002]. Many of the existing T_e estimates for Mars are essentially lower-bound estimates, for several reasons. For example, loads emplaced early in the planetary history do not require further readjustment to maintain isostatic equilibrium as the lithosphere cools and strengthens [*Courtney and Beaumont*, 1983], so the topography and areoid reflect stresses frozen in at the time of loading. Also, some estimates [*McKenzie et al.*, 2002; *Zuber et al.*, 2000; *Turcotte et al.*, 2002] assume surface loading only, resulting in underestimation of the lithospheric strength if net-buoyant internal loads are present [*Forsyth*, 1985; *Nimmo*, 2002]. We examine T_e in the range of 60−200 km in our analysis of Tharsis loading, despite lower estimates reported in some investigations.

Figure 7 depicts the percentage contributions of internal loading to total loading, topography and areoid. We have included solutions using the load limit criterion $\mathcal{L}$=1 (black dots) as well as the convergent solutions for $\mathcal{L}$=∞ (gray dots; i.e., with unlimited load amplitudes). The load estimates exhibit several patterns of dependence on the assumed model parameters. First, one will note that if T_e is about 85 km, the percentage internal contribution to loading (Figure 7a) is negligible for all load depths. Larger values of T_e require a contribution from buoyant internal loading, and the buoyancy of loading increases with increasing depth. For example, a T_e of 120 km would necessitate an 8.4% internal contribution to the vertical lithospheric load stress, a 20.5% internal contribution to topography and a 4.9% internal load contribution to the areoid of Tharsis for a load at 220 km depth. Loading at 420 km would require internal load contributions of 14.1%, 32.6% and 18.2% to loading, topography and areoid respectively if T_e=120 km. On the other hand, a T_e<85 km necessitates internal loading by anomalously dense material, such that for example a 60 km T_e lithosphere loaded

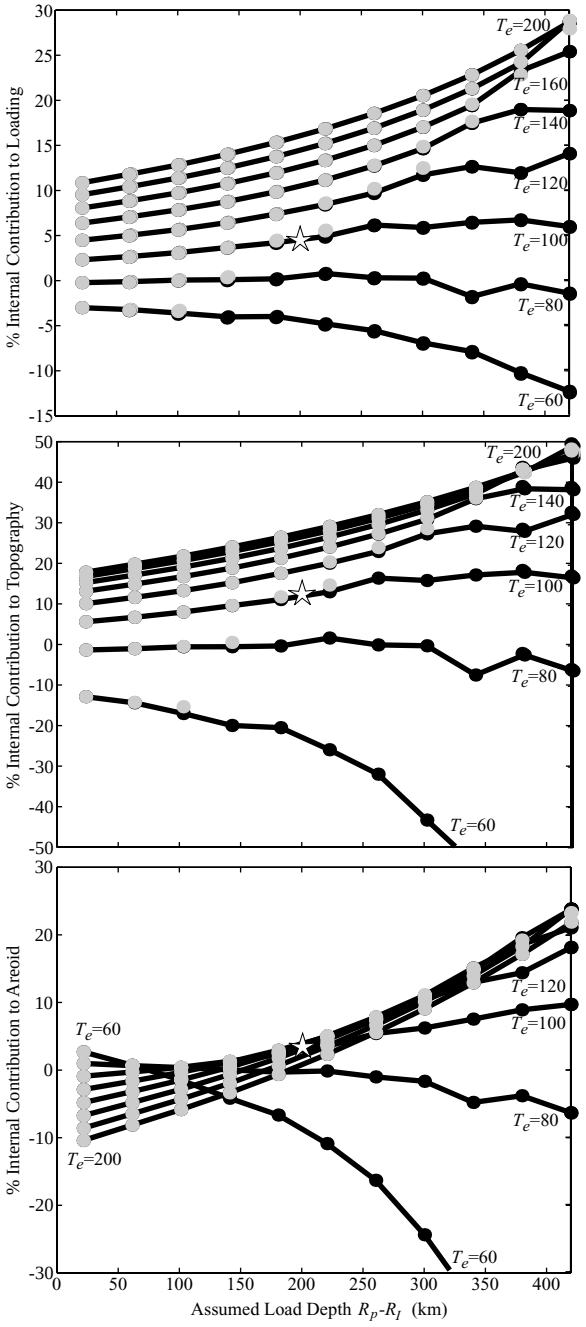

Figure 7. Percentage contribution by internal loading to (a) integrated lithospheric force, (b) topography, and (c) areoid of Tharsis, estimated for T_e=60 to 200 km and depth of internal loading $R_p - R_I$=20 to 420 km. Black circles with solid lines are results using the load limit algorithm (section 2.4) at near-singular load depths; gray circles are convergent solutions with unlimited load coefficients. White star denotes intersection with models of Figure 8.

at 220 km depth would require internal load contributions of -4.9%, -25.7% and -11.0% to lithospheric loading, topography and areoid respectively. The negative contribution of this anomalously dense mass grows with increasing depth of the internal load.

Other uncertain parameters in the estimates of Tharsis loading include crustal thickness T_c and crustal density ρ_0. *Sohl and Spohn* [1997] postulate two models of Martian internal structure derived from meteorite samples of chemical composition, dynamical relations and equations of state. One model, matching the maximum estimate of Martian moment of inertia, yields a mean crustal thickness of 110 km while a second model matching chondritic bulk composition gives 250 km for crustal thickness. *Zuber et al.* [2000] estimate a lower-bound mean thickness of 50 km from the relationship of gravity to topography, and argue that the Martian crustal dichotomy would not be maintained on ∼4Ga timescales if the crust were as thick as 100 km. *Nimmo and Stevenson* [2001] also model flow across the crustal dichotomy using a flow law for dry Columbia diabase, and they estimate the maximum mean crustal thickness to be ∼115 km. However, the viscous flow modeling for both of these upper-bound estimates assumes lower crustal viscosities similar to that of Earth, where silica-rich compositions and deep water cycling processes differ significantly from Martian conditions. Given the pyroxene-rich Martian crustal composition inferred from Shergottite meteorites [*Babeyko et al.*, 1993] and the dependence of diorite creep strength on pyroxene content [*Mackwell et al.*, 1998; *Bystricky and Mackwell*, 2001], Martian lower-crustal strength may exceed that of dry olivine. Such extreme lower crustal strength may readily support the Martian crustal dichotomy over significant timescales. In this analysis, we examine crustal thicknesses (here defined as thickness of crustal material prior to the addition of surface load thickness h^S) in the range of 10−160 km. We also examine a range of crustal densities from 2400 to 3200 kg m^{-3}, encompassing loosely compacted airfall tephras up to the Shergottite crustal composition [*Babeyko et al.*, 1993].

Internal loading contributions for the range of crustal thickness and density are shown in Figure 8, assuming an internal load depth of 200 km and other parameters as listed in Table 2. The buoyancy of the internal load estimate decreases with decreasing crustal density and with decreasing crustal thickness. If we expect a relatively thin crust and low density of fractured or weathered near-surface materials, as suggested by *Nimmo* [2002], the internal buoyancy may be somewhat less than in the calculations shown in Figure 7. If

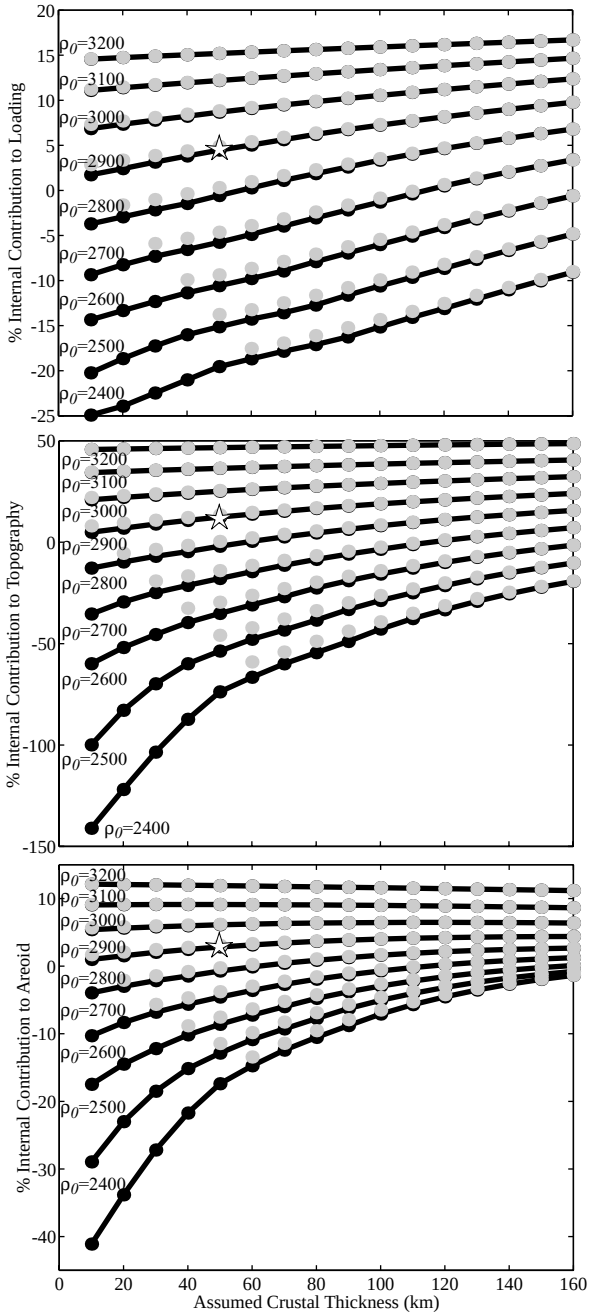

Figure 8. Percentage contribution by internal loading to (a) integrated lithospheric force, (b) topography, and (c) areoid of Tharsis, estimated for ρ_0=2400 to 3200 kg m^{-3} and crustal thickness $R_p - R_1$=10 to 160 km. Black circles with solid lines are results using the load limit algorithm (section 2.4) at near-singular load depths; gray circles are convergent solutions with unlimited load coefficients. White star denotes intersection with models of Figure 7.

on the other hand the crust is thick and crustal density nears the Shergottite composition (ρ ∼3100 kg m^{-3}), as inferred by *Sohl and Spohn* [1997], internal buoyancy (and corresponding contributions to areoid and topography) could be as much as 10% greater than shown in Figure 7.

5. Discussion

Until now, most quantitative estimates of Tharsis loading have assumed *a priori* that loading was either predominantly internal [e.g. *Kiefer et al.*, 1996] or predominantly by surface construction [e.g. *Willemann and Turcotte*, 1982]. Investigations which have explicitly incorporated both surface and internal loading include *Banerdt and Golombek* [2000], which neglects possible viscous coupling to deep loads, and *Zhong and Roberts* [2003], which examined the global expression of l=2−3. Accurate estimates of dynamic loading contributions require a model incorporating both the elastic lithosphere and viscous mantle flow [*Zhong*, 2002]. The method described in this paper factors the elastic lithosphere and viscous flow responses into estimates of the relative contributions of surface and internal loading processes to topographic shape and the geoid. Also, in contrast to power spectral (e.g., "admittance") techniques, this analysis retains all of the information content of the data, including the signs and amplitudes of individual coefficients. Power spectral averaging to estimate the geoid/topography ratio or "admittance", by squaring and summing the coefficients, destroys the location-specific information and moreover strips away much of the coefficient sign information which is crucial to identify the amplitude and sign of loading (e.g., Figure 4). By retaining the information content for each individual coefficient, this method enables analysis of loading processes localized within a particular region of the planet.

We have explored loading estimates within the Tharsis region for a plausible range of parameters, and we find that volcanically constructed surface loads comprise at least 70% of the lithospheric load acting on the Tharsis lithosphere, for $T_e \leq$200 km and internal load depth ≤420 km. For the same parameter range, buoyancy under Tharsis contributes ≤50% of the topographic expression, and ≤25% of the areoid (Figures 7 and 8). *Banerdt and Golombek*'s [2000] model parameterization is virtually identical to that of our reference model (Table 2) except that they use a mantle density of 3500 instead of 3400 kg m^{-3}. They similarly find Tharsis loading to be predominantly surficial, with

an average ∼12 km downward lithospheric deflection w beneath the Tharsis province as compared to 12.7 km for the reference model in section 4.2. The similarity of results is not surprising, given the assumed 50 km loading depth. Viscous stress coupling neglected by *Banerdt and Golombek* [2000] is negligible for loads within the lithosphere. Our upper-bound (25%) estimate of internal contribution to the Tharsis areoid is somewhat larger than the 15% upper-bound cited by *Zhong and Roberts* [2003], but the two analyses differ in some respects. Most notably, *Zhong and Roberts* [2003] assume cooling of the lithospheric between the times of Noachian surface loading and modern plume activity, which reduces the internal contribution to the areoid by reducing T_e at the time of surface loading. Using their assumed model parameterization with T_e=120 km and a load depth of 450 km (corresponding to their upper-bound case), we calculate the internal load contribution to the areoid to be 16.2%. If we limit calculations to the spherical harmonic degrees l=2−3 that they considered, the internal load contribution is 14.8%, virtually identical to their upper-bound estimate.

5.1. Limitations of the load calculation method

The methodology introduced in this paper, while superior to load estimation from power spectra, provides only a range of possible solutions corresponding to the range of uncertainties in model parameters such as the Martian reference density structure, lithospheric thickness and depth of internal loading. The method also incorporates several approximations and assumptions, but these have negligible impact on the results. For example, we use a thin shell approximation to lithospheric strength. Given the thick lithosphere and small planetary radius of Mars, errors in the thin plate approximation can exceed 10% for l>20 [*Zhong and Zuber*, 2000]. However, because of the large areal extent of Tharsis, contributions from higher degrees are negligible. If we perform the calculations using only $l\leq$10, we get results identical to those presented in Figures 7 and 8 (using $l\leq$60) to within a few percent.

We have also neglected the effect of deformation at the core-mantle boundary in the areoid. This approximation is warranted because we limit the internal loading depths to <420 km, for which CMB contributions to the areoid are negligible. Also, the assumption that internal loading occurs at a single fixed radius is one of many possible parameterizations of internal loading. Regardless of how we might choose to specify the depth dependence of loading, a single amplitude parameter describing the internal mass is dictated by the fact that we have only two observables (h and N) at each harmonic. We will explore other depth-dependent parameterizations of buoyancy (e.g., distributions reflecting convective scaling relations) in subsequent analyses.

The algorithm for limiting load amplitudes when the deconvolution matrix is nearly singular (section 2.4) is an important element of the load deconvolution. Limiting the amplitudes at near-singular load depths was necessitated by inclusion of the finite-amplitude areoid response to flexure w (equation 10) in the iterative solution of equations (11). If loads are permitted to be arbitrarily large, w can also be arbitrarily large and the solution of (11) diverges for some combinations of model parameters. If the load deconvolution matrix in equations (11) is nearly singular, but the observed areoid/topography ratio is very different from that predicted for the assumed load depth, the physical implication is that internal loading is probably dominated by mass anomalies at other depths. Nevertheless, we want to represent as accurately as possible the mass distributions predicted for internal loading at a specific planetary radius. In Figures 7 and 8, the gray circles denote convergent solutions obtained without specifying a limit criterion on the maximum load amplitudes (i.e., $\mathcal{L}$=∞). Solutions for those cases which do converge in the absence of a load limit criterion (generally, for combinations of large T_e, shallow internal loading, high crustal density and thick crust) are nearly identical to those obtained using $\mathcal{L}$=1. For results shown in Figure 7, the number of coefficients altered by application of a load limit criterion ranged from 0 for large T_e and shallow loading to ∼350 (out of 1889) for deep internal loading with T_e=60 km.

5.2. Implications for T_e estimation

An important corollary of the method presented here has been noted before [*Forsyth*, 1985]: Namely, any arbitrary choice of T_e and reference density structure can exactly reproduce the relationship of gravity to topography, given an appropriate choice of the relative contributions from surface and internal loading. Consequently, to estimate flexural model parameters such as T_e and density, some assumption or other constraint of the model solution space is required. In *McKenzie et al.* [2002] and *Turcotte et al.* [2002], for example, the solution space is limited by the assumption that loading occurs only at the surface. If, using our methodology, we adopt T_e = 70 km, ρ_0=3000 kg m^{-3} as *McKenzie et al.* [2002] estimate for Tharsis and we adopt their reference density structure, our estimate of internal loading at Tharsis is < 2% for load depths <250 km. Hence,

McKenzie et al.'s [2002] 70 km estimate for T_e of Tharsis is dictated by their assumption that there is no internal loading.

McGovern et al. [2002] incorporate internal loading via a grid search for the T_e and the ratio f of internal loading to surface loading, assumed constant for all (i, l, m), that minimize the difference between observed and predicted admittance functions. They use an unbiased spectral estimate of the complex admittance, which removes via cancellation most of the effects of uncorrelated surface and internal loading present in the data. The modeling assumption of a single constant load ratio f forces the modeled internal load to correlate perfectly with the surface load. Hence, by cancelling uncorrelated load effects and modeling the correlated load, this approach should yield a better approximation of the true T_e than *McKenzie et al.*'s [2002] assumption of no internal loading, unless the correlated load ratio f=0, in which case the two methods are equivalent. However, two significant limitations remain in this approach. For one, there is no guarantee that correlated loading will have constant f-ratio for all (i, l, m) (on the contrary, one would expect processes that correlate surface and internal loads to depend strongly on spatial wavelength). For the second, *McGovern et al.* [2002] explore f only on the interval $[0, 1]$, whereas the potential range is $[-\infty, \infty]$.

McGovern et al. [2002] do not examine Tharsis as a whole, but their estimates for small individual features of Tharsis range from T_e=20−35 km for Highland Plana up to >150 km for Olympus Mons, with most estimates falling in the range 60−100 km. They attribute the variations to age of the load. Their estimates of internal loading are zero for most Tharsis features excepting Alba Patera (f<0.2, corresponding to >17% internal loading in the resolved force estimation used in this paper) and the Valles Marineris (f∼0.5, or ∼33% internal loading). At the 50 km internal load depth assumed in *McGovern et al.* [2002], our estimates of internal loading for all of Tharsis in Figure 7 range from f=−0.04 for T_e=60 km up to f=0.13 for T_e=200 km. Our estimates should not directly equate to theirs owing to differences in the spatial regions examined, their assumption that f is independent of (i, l, m), and ommission of l≤5 (which dominates our loading calculations) by their spatio-spectral localization technique. *Nimmo* [2002] applied a similar fixed-f admittance approach to line-of-sight gravity data over the Martian crustal dichotomy, and estimated T_e of 61±24 km with a best-fit f=1.

All of the estimates of T_e described above are derived from the relationship of the areoid (or gravity) to topography. Because that relationship can be modeled precisely for any arbitrary T_e using equations (11), the accuracy of T_e estimates depends critically on the validity of the assumed relationship between surface and subsurface loading that limits the solution space. The relationship between internal and surface loading processes in the Martian areoid and topography can be examined qualitatively from the ratios of areoid coefficients divided by topography coefficients in the spherical harmonic domain. These coefficient ratios differ from the so-called "geoid-topography ratio" (GTR), in which the squares of coefficients N_{ilm}^2 and h_{ilm}^2 are summed over i, m before dividing. Squaring removes the sign information and hence biases the ratio, so we define an unbiased, amplitude-weighted average coefficient ratio $\bar{R}_l$,

$$\bar{R}_l = \frac{\sum_{i,m} \mathrm{sign}(N_{ilm}/h_{ilm})|N_{ilm}|}{\sum_{i,m} |h_{ilm}|}. \qquad (31)$$

In Figure 9, $\bar{R}_l$ are quite similar to modeled relations for purely surface loading. Most (though not all) of the averaged coefficient ratios fall within a range encompassing the pure surface loading models predicted

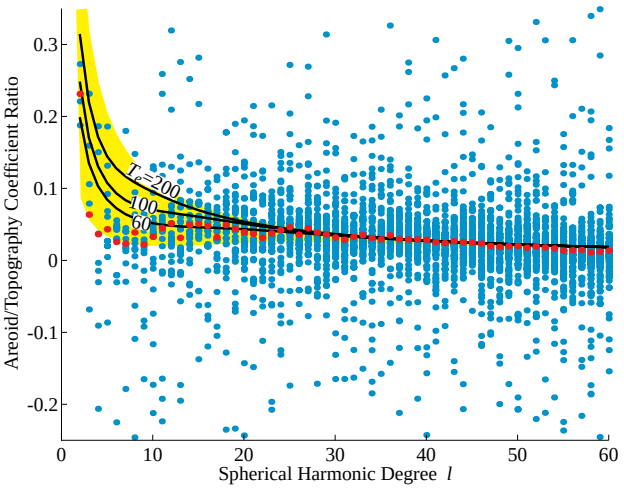

Figure 9. Ratios of areoid/topography coefficients for the data used in this study. Red circles represent ratios $\bar{R}_l$ of coefficients after averaging for given l, and cyan circles are ratios of the individual coefficients. Solid lines are the ratios predicted by pure surface loading using variable T_e as indicated and density model parameters as in Table 2. The yellow region denotes the predicted range of all pure surface loading models encompassing T_e=50−200 km, crustal thickness T_c=10−160 km, ρ_0=2400−3200 kg m^{-3}, and ρ_1=3300−3800 kg m^{-3}.

for a plausible range of T_e and Martian reference density structure. However, individual areoid/topography coefficient ratios, prior to averaging, can deviate significantly from the range for pure surface loading. Eighty-one percent of the individual ratios lie outside the plausible range for surface loading, and fifty-seven percent remain outside that range at 95% confidence when measurement uncertainties are taken into account. Deviation of ratios from the surface load prediction results from a combination of (1) coefficient coupling by finite amplitude effects in the areoid and/or spatially variable lithospheric thickness T_e, and (2) internal loading of the lithosphere. We expect that the distribution of coefficient ratios in Figure 9 is dominated by internal loading. Coincidence of the averaged coefficient ratios with the surface load model prediction suggests that internal loading is an approximately zero-mean process for given l. Such behavior would be expected for randomly distributed, spatially varying density of the planetary interior.

Given that any T_e can be made to exactly fit the areoid and topography data by using equations (11), it is worth examining the assumptions that restrict the solution space for various spherical harmonic domain T_e estimation methods. The assumption by *McKenzie et al.* [2002] and *Turcotte et al.* [2002] that there is no contribution from internal mass anomalies is not consistent with expected scaling of thermal and chemical variations within planetary interiors, nor does it match the large variability in ratio of areoid and topography coefficients for fixed l (Figure 9). Even a small percentage of net contribution from internal mass anomalies can significantly change the estimate of T_e (Figure 7a), so ignoring internal loads is unlikely to yield an accurate estimate.

McGovern et al.'s [2002] and *Nimmo*'s [2002] model assumption that the load ratio f is independent of (i, l, m) implicitly assumes perfect correlation of the loads. Figure 9 clearly demonstrates that loads are not perfectly correlated. For fixed l and fixed depth of loading, a constant f-ratio of internal to surface loading would result in all of the individual coefficient ratios plotting as a single point in Figure 9. However, the unbiased estimate of admittance used in these papers should cancel the uncorrelated components of loading in the "observed" admittance, leaving only that component of internal loading which is correlated with surface loading. When the areoid/topography ratios of global coefficients are averaged in an unbiased fashion using equation (31), we find that the relationship is very similar to a pure surface loading model (i.e., f=0). The small differences between $\bar{R}_l$ and a "best-fit" surface-loading model parameterization are dependent on wavelength, however, in a manner that is not necessarily well-described by a scale-independent parameterization of a correlated surface load ratio f.

5.3. Resolving the T_e ambiguity

A careful description of the ambiguous statistical relationship between surface and internal loading will require the introduction of additional physical constraints and/or other observable quantities into the modeling. Apart from gravity and topography, the most commonly cited observable in studies of Tharsis loading are the associated tectonic structures [*Carr*, 1974; *Willemann and Turcotte*, 1982; *Harder and Christensen*, 1996; *Mege and Masson*, 1996; *Anderson et al.*, 2001; *Banerdt and Golombek*, 2000]. These features reflect the stress/strain fields at the time of their formation, so comparing them to the modern-day areoid and topography may require an evolutionary physical model of Tharsis with substantially more variable parameters than the model described here [*Banerdt et al.*, 1982].

Alternatively, it may be possible to restrict the T_e solution space via careful forward modeling of the loading processes. If degree-one thermal convection is still active, as would seem likely given that Tharsis volcanism has continued to at least the past 100 Myr [*Hartmann et al.*, 1999], internal loading of Tharsis would include significant positive buoyancy. Even if Tharsis single-plume convection is greatly reduced from what it must have once been, chemical buoyancy of basalt-depleted mantle is likely to remain localized within and immediately beneath the Tharsis lithosphere, given the extremely large volumes of basalt which would be required to produce the Tharsis surface loading. Consequently, the Tharsis internal load is much more likely to be net buoyant than anomalously dense. If we conservatively assume a high crustal density (ρ_0=3100 kg m^{-3}) and require that the internal load contribution have a net buoyant contribution, we find that the minimum possible planetary T_e at the time of Tharsis loading is 50 km. The actual T_e can be much larger if the internal load contribution is large, or the crustal density is low. A carefully constructed planetary circulation model, incorporating melt chemistry relations and matching the thermal history requirements for timing of Tharsis volcanism as well as the final ratios of internal to surface loading, could narrow further the possible range of Martian lithospheric thickness.

Until these more complex model spaces can be explored, the distribution of coefficient ratios (Figure 9)

suggests that the statistical relationship of Martian surface and internal loading processes might best be described as uncorrelated, with some instances of locally enhanced correlation that depend strongly on spatial scale. *Forsyth* [1985] hypothesized that randomization by surficial processes such as erosion and deposition should decorrelate surface and internal loads. Hence, *Forsyth*'s [1985] coherence method limits the solution space by choosing the T_e which minimizes correlation of the loads. Erosion and deposition are not the only processes which should decorrelate surface and internal loads. If we remove the effects of isostatic response, most physical process aggregates would tend to have a very different scale dependence for mass redistribution at the surface than at depth. The broad distribution of individual coefficient ratios in Figure 9, with approximately zero-mean relative to the pure surface loading prediction, is consistent with what one would expect to observe if surface and internal loading is uncorrelated. However, some of the averaged coefficient ratios $\bar{R}_l$ (particularly for l<10) are slightly different from the surface load prediction, indicating enhanced correlation of surface and internal loads within wavebands where loading occurs predominantly by coupled processes of volcanism and convection or by extremely large (i.e., Hellas-sized) impacts.

To obtain a preferred estimate of lithospheric thickness and reference density structure of Mars, and hence of the load structure, we examined which of the model parameterizations would minimize the correlation of the surface load estimate h^S with the internal load estimate ξ. The rationale for minimizing the correlation of surface and internal loads (as opposed to modeling the unbiased admittance using a scale-independent load ratio parameterization) is twofold. One reason is that an incorrect load model parameterization will always systematically enhance the apparent correlation of loads calculated via equations (11) by the introduction of (for example) false internal loads that offset, and hence are in phase with, the errors in model estimates of the surface load. Consequently, correlation statistics of the loads are more sensitive to the model parameterization than are the unbiased estimates of admittance. The second reason is that true correlated loads are unlikely to occur everywhere on the planet, nor are they likely to be correlated in a consistent manner at all wavelengths. Indeed, if correlated loads were scale-independent and could simulate the scale dependence of an isostatic model parameter, there would be no advantage to using an admittance estimate because the model parameter and the load ratio f would be completely

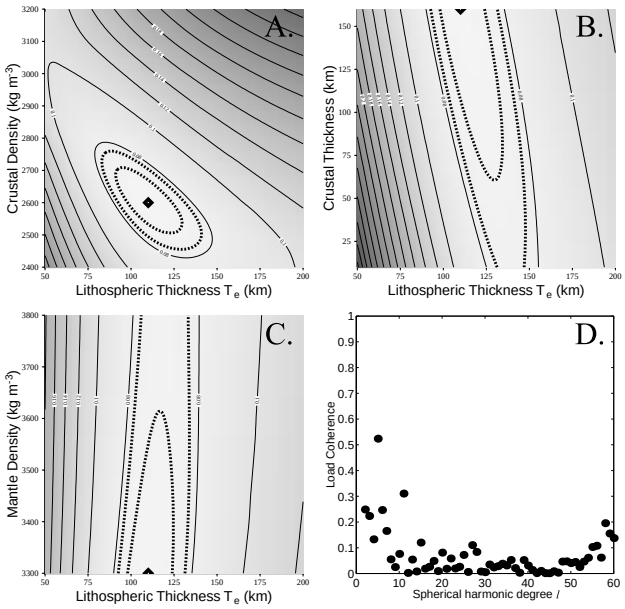

Figure 10. Coherence of the surface load field h^S and internal load ξ as a function of assumed model parameters. The contour interval is 0.02, the 65% and 95% confidence ellipses for the minimum are shown as thick dotted lines, and the minimum coherence is indicated by a diamond. (a) Lithospheric thickness T_e versus crustal density ρ_0. (b) Lithospheric thickness T_e versus crustal thickness T_c. (c) Lithospheric thickness T_e versus mantle density ρ_1. (d) Coherence as a function of spherical harmonic degree l for the minimum global γ^2 defined by T_e=110 km, ρ_0=2600 kg m^{-3}, T_c=160 km, and ρ_1=3300 kg m^{-3}.

cross-correlated in any grid-search minimization of the difference between model and observation. Hence, although loading will be somewhat correlated on certain spatial scales at some locations, the optimal model parameterization is in any case likely to be that which minimizes the global correlation of loads estimated via equations (11).

In Figure 10, we show the averaged global coherence γ^2 between surface and internal loads,

$$\gamma^2 = \frac{1}{59}\sum_{l=2}^{60} \frac{\left|\sum_{m=0}^{l}(h^S_{1lm} + \imath h^S_{2lm})(\xi_{1lm} - \imath\xi_{2lm})\right|^2}{\sum_{i,m}(h^S_{ilm})^2 \sum_{i,m}\xi^2_{ilm}}, \tag{32}$$

for a range of assumed lithospheric thickness T_e, crustal density ρ_0, crustal thickness T_c, and mantle density ρ_1. A grid search over these parameters, assuming other parameters as given in Table 2 and a 50 km load depth,

yields a global minimum coherence of the load fields γ^2=0.071 when T_e=110 km, ρ_0=2600 kg m^{-3}, T_c=160 km and ρ_1=3300 kg m^{-3}. Note that it is desirable to assume a shallow load depth for this calculation, as assuming a deep internal load can dramatically amplify (and spuriously correlate) the load coefficients for assumed load depths approaching the singular depth. Also shown as thick dotted lines in Figure 10 are the 65% and 95% confidence intervals for the parameters that yield minimum coherence, estimated via the likelihood ratio method [*Beck and Arnold*, 1977]. The minimum-coherence parameters of T_e and ρ_0 are tightly constrained, but the coherence of estimated loads is so insensitive to assumed T_c and ρ_1 that no value in the range of the search can be rejected at high confidence.

The coherence as a function of spherical harmonic degree l for the model parameterization that minimizes equation (32) is also shown in Figure 10d. The coherence is non-negligible at $l \leq 10$ and $l > 50$, where averaged coefficient ratios show evidence of bias downward from the surface load prediction (Figure 9). Increased coherence of surface and internal loading at the very long wavelengths may result from the collocation of volcanic loading and thermal/chemical buoyancy at Tharsis and Elysium, as well as crustal excavation and mantle upwarp by the Hellas and Utopia impacts. Increased correlation of surface and internal loads at $l > 50$ may reflect surface density at the major volcanoes (Olympus, Pavonis, Ascraeus, Arsia, Syrtis Major and Syria Planum) which dominate the areoid and topographic power at these wavelengths. These features likely have much higher density than the 2600 kg m^{-3} which best represents the remainder of the Martian topography. The residual mass of the volcano edifice would be assigned to subsurface loading by the solution of equations (11) and then amplified by downward continuation to 50 km depth.

If we assume the parameters that minimize coherence represent a "best" approximation of the Martian lithosphere and density structure, we can also calculate a preferred estimate of the internal contribution to loading of Tharsis. Using the minimum coherence parameters and an internal load depth of 200 km, we find that the internal buoyancy contributes 2.1% of the lithospheric force balance, 4.2% of the topography and 0.7% of the areoid at Tharsis.

6. Conclusions

We have introduced a methodology for inverting internal and surface loading effects from geoid and topography data. The method incorporates the physics of both lithospheric stress and viscous coupling to deeper loads, as well as finite amplitude effects of layer boundary topography on the geoid. Application of the method to synthetic geoid and topography outputs from a fully viscoelastic formulation of planetary loading [*Zhong and Zuber*, 2000] yields negligible errors of <5% in recovery of the input loads.

The method was applied to estimate loading of the Tharsis province on Mars. By far the largest uncertainties in the contribution of internal loading to Tharsis are introduced by parameter uncertainties in the depth of internal loading, lithospheric thickness, and reference density structure of Mars.

Within parameter uncertainties, lithospheric loading by internal buoyancy beneath Tharsis is less than half of that by volcanically constructed surface loads. Internal buoyancy is responsible for $\leq$50% of the topographic expression of Tharsis, and $\leq$25% of the areoid (Figures 7 and 8). The upper-bound estimate of internal load contribution would require deep internal loading $\sim$420 km, a thick lithosphere $T_e \sim$200 km, and a high crustal density near 3000 kg m^{-3}. We cannot rule out a null contribution from the internal Tharsis load, nor can we rule out negative contributions from an anomalously dense load.

Using the methodology developed here, the relationship between geoid and topography can be modeled exactly using any arbitrarily chosen T_e and reference density structure. Hence, when estimating a "best" T_e and density from gravity and topography, it is necessary to somehow constrain the stochastic relationship between surface and internal loading. Distributions of individual areoid/topography coefficient ratios (Figure 9) suggest that the relationship between surface and internal loads is best (albeit not perfectly) described as uncorrelated. If that assessment is correct, T_e and density can be estimated by minimizing the global coherence of surface and internal load estimates. We find that coherence is minimized at 95% confidence by a lithospheric thickness T_e=110$\pm$30 km and crustal density ρ_0=2600$\pm$150 kg m^{-3} (Figure 10). Load coherence is also minimized by crustal thickness T_c=160 km and mantle density ρ_1=3300 kg m^{-3}, but it is insensitive to these parameters at 95% confidence.

Using the minimum-coherence parameters and an internal load depth of 200 km, internal buoyancy contributes 2.1% of the lithospheric force balance, 4.2% of the topography and 0.7% of the areoid at Tharsis. For the same parameterization with a load depth of 400 km, internal buoyancy contributes 4.3% of the litho-

spheric force balance, 8.5% of the topography and 2.2% of the areoid at Tharsis. Internal load contributions for other model parameterizations can be determined from inspection of Figures 7 and 8.

Acknowledgments. We thank Frank Lemoine of Goddard Space Flight Center for providing the GMM-2B areoid and associated degree variances, and Sean Swenson at the University of Colorado for his algorithms for spherical harmonic transformation and optimal mass averaging. Isabella Velicogna offered valuable discussion and advice, and the manuscript was greatly improved by constructive suggestions from Jeroen van Hunen and Francis Nimmo, as well as referees Bruce Banerdt and Oded Aharonson. Some of the figures were produced using GMT [*Wessel and Smith*, 1998]. This research was supported by NASA's Mars Global Surveyor Data Analysis Program grant NAG5-11224 and the David and Lucile Packard and Alfred P. Sloan Foundations.

References

Anderson, R. C., J. M. Dohm, M. P. Golombek, A. F. C. Haldemann, B. J. Franklin, K. L. Tanaka, J. Lias, and B. Peer, Primary centers and secondary concentrations of tectonic activity through time in the western hemisphere of Mars, *J. Geophys. Res.*, *106*, 20,563–20,585, 2001.

Babeyko, A. Y., S. V. Sobolev, and V. N. Zharkov, On mineralogical and velocity structure of the Martian crust, *Astron. Vestn.*, *27*, 55–75, 1993.

Banerdt, W. B., and M. P. Golombek, Tectonics of the Tharsis region of Mars: Insights from MGS topography and gravity, *Proc. Lunar Planet. Sci. Conf.*, *31*, abstr. #2038, 2000.

Banerdt, W. B., R. J. Phillips, N. H. Sleep, and R. Saunders, Thick shell tectonics on one-plate planets: Applications to Mars, *J. Geophys. Res.*, *87*, 9723–9733, 1982.

Beck, J. V., and K. J. Arnold, *Parameter Estimation in Engineering and Science*, John Wiley, New York, 1977.

Bills, B. G., and T. S. James, Moments of inertia and rotational stability of Mars: Lithospheric support of subhydrostatic rotational flattening, *J. Geophys. Res.*, *104*, 9081–9096, 1999.

Breuer, D., D. A. Yuen, T. Spohn, and S. Zhang, Three-dimensional models of Martian mantle convection with phase transitions, *Geophys. Res. Lett.*, *25*, 229–232, 1998.

Bystricky, M., and S. Mackwell, Creep of dry clinopyroxene aggregates, *J. Geophys. Res.*, *106*, 13,443–13,454, 2001.

Carr, M. H., Tectonism and volcanism of the Tharsis region of Mars, *J. Geophys. Res.*, *79*, 3943–3949, 1974.

Courtney, R. C., and C. Beaumont, Thermally-activated creep and flexure of the oceanic lithosphere, *Nature*, *305*, 201–204, 1983.

Forsyth, D. W., Subsurface loading estimates of the flexural rigidity of continental lithosphere, *J. Geophys. Res.*, *90*, 12,623–12,632, 1985.

Hager, B. H., and M. A. Richards, Long-wavelength variations in Earth's geoid: Physical models and dynamical implications, *Phil. Trans. Roy. Soc. Lond. A*, *328*, 309–327, 1989.

Harder, H., Mantle convection and the dynamic geoid of Mars, *Geophys. Res. Lett.*, *27*, 301–304, 2000.

Harder, H., and U. Christensen, A one-plume model of Martian mantle convection, *Nature*, *380*, 507–509, 1996.

Hartmann, W. K., M. Malin, A. McEwen, M. Carr, L. Soderblom, P. Thomas, E. Danielson, P. James, and J. Veverka, Evidence for recent volcanism on Mars from crater counts, *Nature*, *397*, 586–589, 1999.

Kiefer, W. S., Gravity evidence for extinct magma chambers on Mars: Tyrrhena Patera and Hadriaca Patera, *Proc. Lunar Planet. Sci. Conf.*, *34*, abstr. #1234, 2003.

Kiefer, W. S., B. G. Bills, and R. S. Nerem, An inversion of gravity and topography for mantle and crustal structure on Mars, *J. Geophys. Res.*, *101*, 9239–9252, 1996.

Lemoine, F. G., D. E. Smith, D. D. Rowlands, M. T. Zuber, G. A. Neumann, D. S. Chinn, and D. E. Pavlis, An improved solution of the gravity field of Mars (GMM-2B) from Mars Global Surveyor, *J. Geophys. Res.*, *106*, 23,359–23,376, 2001.

Lowry, A. R., N. M. Ribe, and R. B. Smith, Dynamic elevation of the Cordillera, western United States, *J. Geophys. Res.*, *105*, 23,371–23,390, 2000.

Mackwell, S. J., M. E. Zimmerman, and D. Kohlstedt, High temperature deformation of dry diabase with application to tectonics on Venus, *J. Geophys. Res.*, *103*, 975–984, 1998.

McGovern, P. J., et al., Localized gravity/topography admittance and correlation spectra on Mars: Implications for regional and global evolution, *J. Geophys. Res.*, *107*, doi:10.1029/2002JE001,854, 2002.

McKenzie, D., D. N. Barnett, and D. N. Yuan, The relationship between Martian gravity and topography, *Earth Planet. Sci. Lett.*, *195*, 1–16, 2002.

Mege, D., and P. Masson, A plume tectonics model for the Tharsis province, Mars, *Planet. Space Sci.*, *44*, 1499–1546, 1996.

Nimmo, F., Admittance estimates of mean crustal thickness and density at the Martian hemispheric dichotomy, *J. Geophys. Res.*, *107*, doi:10.1029/2000JE001,488, 2002.

Nimmo, F., and D. J. Stevenson, Estimates of Martian crustal thickness from viscous relaxation of topography, *J. Geophys. Res.*, *106*, 5085–5098, 2001.

Phillips, R. J., et al., Ancient geodynamics and global-scale hydrology on Mars, *Science*, *291*, 2587–2591, 2001.

Sleep, N. H., and R. J. Phillips, An isostatic model for the Tharsis province, Mars, *Geophys. Res. Lett.*, *6*, 803–806, 1979.

Smith, D. E., W. L. Sjogren, G. L. Tyler, G. Balmino, F. G. Lemoine, and A. S. Konopliv, The gravity field of Mars: Results from Mars global surveyor, *Science*, *286*, 94–97, 1999b.

Smith, D. E., et al., The global topography of Mars and implications for surface evolution, *Science*, *284*, 1495–1503, 1999a.

Sohl, F., and T. Spohn, The interior structure of Mars: Implications from SNC meteorites, *J. Geophys. Res.*, *102*, 1613–1635, 1997.

Solomon, S. C., and J. W. Head, Evolution of the Tharsis province of Mars: The importance of heterogeneous lithospheric thickness and volcanic construct, *J. Geophys. Res.*, *87*, 9755–9774, 1982.

Swain, C. J., and J. F. Kirby, The effect of noise on estimates of the elastic thickness of the continental lithosphere by the coherence method, *Geophys. Res. Lett.*, *in press*, 2003.

Swenson, S., and J. Wahr, Methods for inferring regional surface-mass anomalies from GRACE measurements of time-variable gravity, *J. Geophys. Res.*, *107*, doi:10.1029/2001JB000,576, 2002.

Tanaka, K. L., M. P. Golombek, and W. B. Banerdt, Reconciliation of stress and structural histories of the Tharsis region of Mars, *J. Geophys. Res.*, *96*, 15,617–15,633, 1991.

Tanaka, K. L., D. H. Scott, and R. Greeley, Global stratigraphy, in *Mars*, edited by H. H. K. et al., pp. 345–382, Univ. of Ariz. Press, Tucson, 1992.

Turcotte, D. L., R. J. Willeman, W. F. Haxby, and J. Norberry, Role of membrane stresses in the support of planetary topography, *J. Geophys. Res.*, *86*, 3951–3959, 1981.

Turcotte, D. L., R. Shcherbakov, B. D. Malamud, and A. B. Kucinskas, Is the Martian crust also the Martian elastic lithosphere?, *J. Geophys. Res.*, *107*, doi:10.1029/2001JE001,494, 2002.

Wessel, P., and W. H. F. Smith, New, improved version of Generic Mapping Tools released, *Eos Trans. AGU*, *79*, 579, 1998.

Wieczorek, M. A., and R. J. Phillips, Potential anomalies on a sphere: Applications to the thickness of the lunar crust, *J. Geophys. Res.*, *103*, 1715–1724, 1998.

Willemann, R. J., and D. L. Turcotte, The role of lithospheric stress in the support of the Tharsis rise, *J. Geophys. Res.*, *87*, 9793–9801, 1982.

Zhong, S., Dynamics of crustal compensation and its influences on crustal isostasy, *J. Geophys. Res.*, *102*, 15,287–15,299, 1997.

Zhong, S., Effects of lithosphere on the long-wavelength gravity anomalies and their implications for the formation of the Tharsis rise on Mars, *J. Geophys. Res.*, *107*, doi:10.1029/2001JE001,589, 2002.

Zhong, S., and J. H. Roberts, On the support of the Tharsis rise on Mars, *Earth Planet. Sci. Lett.*, *submitted*, 2003.

Zhong, S., and M. T. Zuber, Long-wavelength topographic relaxation for self-gravitating planets and its implications to the compensation of lunar basins, *J. Geophys. Res.*, *105*, 4153–4164, 2000.

Zuber, M. T., et al., Internal structure and early thermal evolution of Mars from Mars Global Surveyor topography and gravity, *Science*, *287*, 1788–1793, 2000.

This preprint was prepared with AGU's LaTeX macros v5.01, with the extension package 'AGU++' by P. W. Daly, version 1.6b from 1999/08/19.